



# Multi-objective Shape Optimization of Airfoils for Mars Exploration Aircraft Propellers

Kitae Park<sup>1</sup> · Jongho Jung<sup>2</sup> · Shinkyu Jeong<sup>1</sup>

Received: 31 March 2022 / Revised: 31 March 2022 / Accepted: 29 July 2022 / Published online: 21 August 2022  
© The Author(s), under exclusive licence to The Korean Society for Aeronautical & Space Sciences 2022

## Abstract

This study aims to improve the aerodynamic performance of a propeller for Mars exploration aircraft by applying multi-objective shape optimization to its airfoils. To increase the accuracy of performance evaluation in the low-Reynolds-number and high-subsonic flows condition on Mars, a Reynolds-averaged Navier–Stokes simulation using the  $\gamma$ - $Re_{\theta}$  transition model, which can predict the laminar separation bubble and the location of the laminar–turbulent transition with high accuracy, is employed. Furthermore, multi-objective shape optimization is performed using a shape-definition method with a high degree of freedom to enable the inclusion of a variety of airfoil shapes. A multi-objective genetic algorithm is used to determine the optimal airfoil shape, and a Kriging model is used to reduce the computation time. The Adkins method is used to determine the optimal shape of the propeller using the designed airfoil. Then, the performance and efficiency of the propeller are investigated. Results demonstrate improvements in the power consumption and efficiency of the propeller using the designed airfoil over those of the propellers using reference airfoils. Quantitative and qualitative correlations between the design variables and airfoil performance are also analyzed using analysis of variance and self-organizing map methods to extract the geometric features that affect airfoil performance.

**Keywords** Propeller design · Mars exploration aircraft · MOGA · Aerodynamics · Optimization · Data mining

## 1 Introduction

Mars is one of the most important targets for planetary exploration, and a number of countries, including the United States, Russia, and European countries, have sent satellites, landers, and rovers to the planet since the 1960s. Most of the Mars exploration techniques attempted so far are of two types: and orbital exploration using satellites and surface exploration using landers and rovers. Orbital exploration offers the advantage of observing a much wider area while being limited by the acquisition of low-resolution data. Conversely, landers and rovers obtain high-resolution surface and atmospheric data, but their range of exploration is relatively limited because they are either fixed to one place or move at slow speeds. In addition, landers and rovers experience

difficulties in accessing rugged terrain. To overcome these issue, the Mars rotorcraft was developed to compensate for the low data resolution of orbital exploration vehicles and for the narrow range of surface exploration devices [1–4]. In April 2021, the NASA Ingenuity successfully completed its first flight on Mars, strongly signaling the possibility of operating heavier-than-air flying vehicles in the Martian region of Seitha, whose rugged terrain is known for difficulty to access using rovers. Nevertheless, this rotorcraft has a limited power supply, which only permits a narrow range of exploration with a small payload.

Another exploration method that can be used to overcome the limitations of the aforementioned rotorcraft involves the use of a fixed-wing aircraft. This vehicle has the advantage of being able to explore rough terrain over a wide range of hundreds to thousands of kilometers while acquiring data with a relatively high resolution. For the development of fixed-wing aircraft for this purpose, the United States launched the Airplane for Mars Exploration (AME) mission in 1996 [5]. This was followed by various research projects, such as the Aerial Regional-Scale Environmental Survey (ARES) project [6] and the Preliminary Research Aerodynamic Design to Land

✉ Shinkyu Jeong  
icarus@khu.ac.kr

<sup>1</sup> Department of Mechanical Engineering, Kyunghee University, Yongin, Korea

<sup>2</sup> Department of Aerospace Engineering, Seoul National University, Seoul, Korea

of Mars (Prandtl-m) project. In Japan, as part of the Mars Exploration of Lift Organism Search (MELOS) mission, the research and development of a Mars exploration aircraft is currently in progress [7]. The present author's research group is also conducting a study on the development of a Mars exploration aircraft [8].

The most difficult aspect concerning the development of a Mars exploration aircraft is that the density of the Martian atmosphere is approximately 1% of that of the Earth's atmosphere. In addition, since the Martian atmosphere is primarily composed of CO<sub>2</sub>, the air temperature and specific heat ratio are lower than those of Earth, while the speed of sound is approximately 0.7 times that of the Earth's atmosphere. Due to these properties, flight conditions on Mars are characterized by very low Reynolds numbers and high-subsonic flows.

In low-Reynolds-number flows, the magnitude of the lift generated by the airfoil and wing is significantly reduced [9, 10]. As the maximum lift coefficient of the airfoil decreases and the drag coefficient increases, the airfoil shape that offers optimum aerodynamic performance becomes very different from the corresponding shape observed in the higher-Reynolds-number flows on Earth. Considering such properties of low-Reynolds-number flows, several studies have been conducted to develop airfoils that can generate sufficient lift and propulsion for flight in the Martian atmosphere. Smith et al. [11] evaluated the performance of a family of airfoils using 2D and 3D Navier–Stokes simulations to select an airfoil suitable for ARES aircraft while also investigating their geometric characteristics. Oyama et al. [12] designed the airfoils of Mars exploration aircraft using 2D Reynolds-averaged Navier–Stokes (RANS) simulations and evolution algorithms. Anyoji et al. [13, 14] evaluated airfoil performance in low-Reynolds-number flows using Mars wind tunnel to simulate the Martian atmosphere. Datta et al. used XFOIL to design a rotor-blade airfoil for a Martian rotorcraft. However, even though XFOIL is widely used for rotor and propeller design, it cannot accurately predict airfoil performance considering the laminar separation bubble and the location of the laminar–turbulent transition in low-Reynolds-number flows; this is because it uses the  $e^N$  method, which determines this transition using the semi-empirical parameter  $N$ .

A laminar separation bubble is created when the laminar flow is separated in the region of an adverse pressure gradient on the airfoil. This separated free shear layer is unstable and amplifies the Tollmien–Schlichting (TS) instabilities. It generally transitions rapidly from laminar to turbulent flow, after which it gets reattached to the airfoil. The separation bubble increases the drag and nonlinearity of the lift curve. Therefore, it is essential to accurately predict the formation of the laminar separation bubble to evaluate the aerodynamic performance of airfoils in low-Reynolds-number flows. Moreover, in such flows, the location of

laminar–turbulent transition has a significant effect on the skin friction. For example, moving the transition point in the leading-edge direction by 20% increases the skin friction by 24.5% [15]. Therefore, it is also essential to accurately predict this location to achieve an accurate evaluation of the airfoil drag in such flows. Towards this end, Koning et al. [16] investigated the optimization of the lift-to-drag ratio of a Martian rotor airfoil with a cambered thin-plate shape using RANS simulations with the SA-AFT2017b transition model. However, to achieve a stable and sustainable flight on Mars, it is necessary to evaluate not only the lift-to-drag ratio but also the stability of the airfoil performance. Furthermore, a cambered thin plate has a low degree of freedom; this necessitates the exploration of other shapes for the airfoil. For this purpose, a shape-definition method with a high degree of freedom is required to consider airfoils of various shapes.

Recently, data mining [17–20] has attracted a great deal of attention as a promising tool for analysis for data obtained during the design process. Data mining is the process of analyzing data and transforming it into useful information. The information obtained by data mining can supply insight into the design of complex systems and help define a suitable formulation of the design problem. It also gives a clue of understanding why the solution obtained by optimization design has an improved performance.

In this study, multi-objective shape optimization of the airfoil for the propeller of Mars exploration aircraft is conducted to design the propeller which has a good aerodynamic performance under conditions of the low-Reynolds-number and high-subsonic flow on Mars. To consider the various shapes of an airfoil, a shaped-definition method with a high degree of freedom is adopted. Airfoil shapes were explored, and the optimal shape was determined using a multi-objective genetic algorithm (MOGA), while a Kriging model was used to reduce the computation time. To evaluate the performance of propeller based on the designed airfoil, the Adkins method was used to determine the propeller shape. The main contributions of this study can be summarized as follows:

1. The compressible RANS-based computational flow dynamics (CFD) simulation using  $\gamma$ - $Re_\theta$  transition model which can predict the laminar separation bubble and the location of the laminar–turbulent transition is employed to evaluate the aerodynamic performance under conditions of the low-Reynolds-number high-subsonic flow on Mars accurately. The difference between the efficiency (or required power) of propeller designed by the database constructed using the high-fidelity solver (RANS simulation using  $\gamma$ - $Re_\theta$  transition model) and that of propeller designed by the database constructed using XFOIL is investigated.

2. The quantitative and qualitative correlations between the design variables and airfoil performance were analyzed using data mining tools (the analysis of variance (ANOVA) [21] and self-organizing map (SOM) methods [22])

This paper is organized as follows: In Sect. 2, the numerical methods used for the RANS-based computational flow dynamics (CFD) simulation using  $\gamma$ - $Re_\theta$  transition model is described. Section 3 presents the propeller design method used to optimize the propeller shape based on the designed airfoil. In Sect. 4, multi-objective optimization for the propeller airfoil, results of the propeller design, and data mining are presented. Finally, the conclusion of this study is given in Sect. 5.

## 2 Numerical Method

In this study, the Tohoku University Aerodynamic Simulation code–Parallel Unstructured Grid (TAS–PUG) code was used to evaluate the aerodynamic performance of the airfoils [23]. TAS–PUG solves the compressible RANS equation using the cell vertex finite-volume scheme. For numerical flux calculations, the Harten–Lax–van Leer–Einfeldt–Wada (HLLIW) approximate Riemann solver is used. Second-order spatial accuracy is realized with a linear reconstruction of the primitive variables inside the control volume with Venkatakrishnan’s limiter [24]. For time integration, the lower/upper symmetric Gauss–Seidel (LU–SGS) implicit method [25] for unstructured meshes is used.

The  $k$ – $\omega$  shear stress transport (SST) and the  $\gamma$ - $Re_\theta$  models [26–28] are used as the turbulence and transition models, respectively. The  $\gamma$ - $Re_\theta$  model uses two transport equations, wherein each equation calculates the intermittency and transition onset momentum thickness Reynolds number. If the flow transitions from the laminar to the turbulent regime, the  $\gamma$  value at that position changes from 0 to 1; this can be used to determine the location of transition.

Figure 1 shows the grid used for calculations in this study. An unstructured hybrid grid was employed with 25 layers of prism grids constructed near the wall to ensure the accurate calculation of boundary layers on the wall of the airfoil. The  $y^+$  value at 50% of the chord length is approximately 0.9. In addition, the far-field boundary was constructed using a length that is 25 times that of the chord length, and the number of grid points is approximately 40,000. Grid dependency was analyzed by changing the grid size under flow conditions corresponding to a Reynolds number of 100,000, a Mach number of 0.2, and an angle of attack of  $4^\circ$ . As can be seen in Fig. 2, the lift and drag coefficients converged to within 0.4%, relative to one utilizing a greater number of grid points.

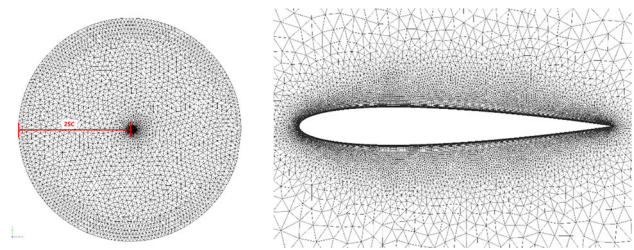


Fig. 1 Computational grid surrounding NACA0012 airfoil

To validate the turbulence and transition models used in this study, the flow field around the NACA0012 airfoil at  $Re = 100,000$ ,  $M = 0.2$ , and  $\alpha = 4^\circ$  was calculated using XFLR5 with the  $e^N$  method, the  $k$ – $\omega$  SST model, and the  $\gamma$ - $Re_\theta$  transition model; the results of these calculations were compared with those of direct numerical simulation (DNS) [29, 30]. Figure 3 shows the  $C_p$  and  $C_f$  obtained from each calculation. Table 1 summarizes the separation, transition, and reattachment positions. The result of the  $\gamma$ - $Re_\theta$  transition model is similar to that of the DNS, while the results of the other models do not display such adequate predictions. Thus, the RANS-based computational flow dynamics (CFD) simulations using the  $\gamma$ - $Re_\theta$  transition model is used for the performance evaluation of airfoil operated under conditions of the low-Reynolds-number and high-subsonic flows on Mars in this study.

## 3 Propeller Design Method

In this study, the propeller design method suggested by Adkins et al. [31] was used to optimize the propeller shape based on the given airfoil. This method combines the use of two theories. The first is the momentum theory [32], which assumes the propeller to be a single disk and interprets its performance in terms of the momentum difference generated in the flow passing over its surface. The second is the blade element theory [33], which analyzes the performance of the propeller by dividing it into small elements in the radial direction while considering the force generated by each element and the circulation due to them. With these theories, the method finds the propeller shape inversely which satisfies the Betz condition for minimum energy loss [34] and the required performance (Thrust or power) according to the design procedure shown in Fig. 4. The detailed inverse design procedure is as follows:

Step 1: The design is started with the given propeller specification such as free stream velocity ( $V$ ), angular velocity ( $\Omega$ ), propeller radius ( $R$ ), number of blades ( $N_B$ ), density of air ( $\rho$ ) and required Thrust ( $T$ ) (or Power ( $P$ )).

Step 2: Select an initial value for the displacement velocity ratio  $\zeta$  (usually,  $\zeta$  is set to zero.)

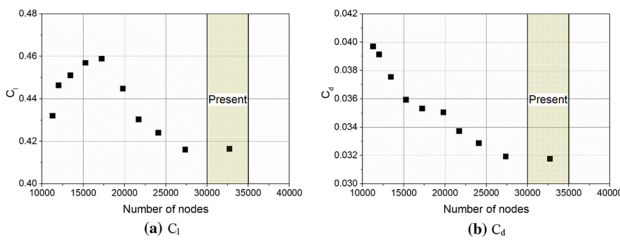


**Fig. 2** Grid dependency of  $C_1$  and  $C_d$  for NACA0012 airfoil

Step 3: Determine the values for the Prandtl momentum loss factor ( $F$ ) and the flow angle ( $\phi$ ) at each blade station by following equations:

$$F = \frac{2}{\pi} \cos^{-1}(e^{-f}), \tag{1}$$

$$f = \frac{N_B}{2} (1 - \xi) / \sin \phi_t, \tag{2}$$

$$\tan \phi_t = \lambda \left( 1 + \frac{\xi}{2} \right), \tag{3}$$

$$\tan \phi = (\tan \phi_t) / \xi, \tag{4}$$

where  $\phi_t$ ,  $\lambda$ ,  $\xi$  are flow angle at the tip, speed ratio ( $= V/\Omega R$ ) and nondimensional radius ( $= r/R$ ), respectively.

Step 4: Determine the product of local total velocity ( $W$ ) and blade chord length ( $c$ ), and Reynolds number ( $Re$ ) from the following Equations.

$$Wc = \frac{4\pi V^2 F x \cos \phi \sin \phi \xi}{(C_1 N_B \Omega)}, \tag{5}$$

$$Re = \frac{Wc}{\nu}, \tag{6}$$

where  $x (= \Omega r/V)$  is nondimensional distance and  $C_1$  is blade section lift coefficient.  $\nu$  is dynamic viscosity.

Step 5: Under the given flow condition ( $V$  and  $Re$  obtained in step 4), find  $C_1$  and angle of attack ( $\alpha$ ), where the minimum drag-to-lift ratio ( $\varepsilon$ ) is obtained at each blade station by using the aerodynamic database of a given airfoil. If  $C_1$  obtained is different from the  $C_1$  used in step 4,  $Re$  should be adjusted. Repeat Step 4 and 5 until it is converged at each station. Thus, basically, the propeller with a better lift-to-drag performance airfoil has a better propeller performance in the present method.

Step 6: Determine the axial interference factor ( $a$ ) and the rotational interference factor ( $a'$ ), and  $W$  from the following equations (See Fig. 5 for the flow geometry at blade station

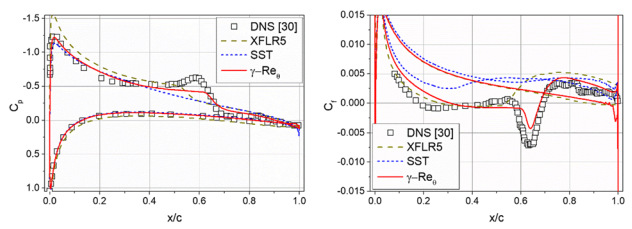


**Fig. 3** Comparison of  $C_p$  and  $C_f$

**Table 1** Comparison of the separation, transition, and reattachment positions

Model	Separation	Transition	Reattachment
DNS [30]	0.20	0.63	0.68
XFLR5	0.26	0.52	0.54
$k-\omega$ SST	–	–	–
$\gamma-Re_\theta$	0.31	0.64	0.68

$r)$ :

$$a = \frac{\xi}{2} \cos^2 \phi (1 - \varepsilon \tan \phi), \tag{7}$$

$$a' = \frac{\xi}{2x} \cos \phi \sin \phi \left( 1 + \frac{\varepsilon}{\tan \phi} \right), \tag{8}$$

$$W = V(1 + a) / \sin \phi. \tag{9}$$

Step 7: Find the blade chord length ( $c$ ) from Eq. (5), and the blade twist  $\beta = \alpha + \phi$ .

Step 8: Determine the four derivatives in I and J from the following Equations and integrate these from  $\xi = \xi_0$  (propeller hub) to  $\xi = 1$  (tip).

$$I_1' = 4\xi G (1 - \varepsilon \tan \phi), \tag{10}$$

$$I_2' = \lambda \left( \frac{I_1'}{2\xi} \right) \left( 1 + \frac{\varepsilon}{\tan \phi} \right) \sin \phi \cos \phi, \tag{11}$$

$$J_1' = 4\xi G \left( 1 + \frac{\varepsilon}{\tan \phi} \right), \tag{12}$$

$$J_2' = \left( \frac{J_1'}{2} \right) (1 - \varepsilon \tan \phi) \cos^2 \phi, \tag{13}$$

where  $G = F x \cos \phi \sin \phi$ .

Step 9: When required thrust is given, calculate  $\zeta$  and the power coefficient ( $P_c$ ) using the following equations:

$$\zeta = \left( \frac{I_1}{2I_2} \right) - \sqrt{\left( \frac{I_1}{2I_2} \right)^2 - \frac{T_c}{I_2}}, \tag{14}$$

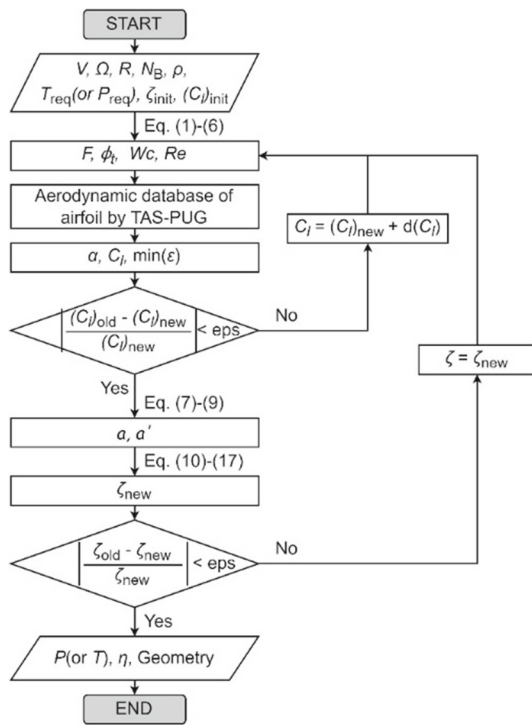


Fig. 4 Flowchart of the propeller design method in this study

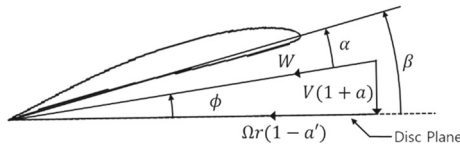


Fig. 5 Flow geometry at blade station  $r$

$$P_c = J_1 \zeta + J_2 \zeta^2, \tag{15}$$

where  $T_c = 2T / (\rho V^2 \pi R^2)$ . Otherwise, when required power is given, calculate  $\zeta$  and the thrust coefficient ( $T_c$ ) using the following equations:

$$\zeta = -\left(\frac{J_1}{2J_2}\right) + \sqrt{\left(\frac{J_1}{2J_2}\right)^2 + \frac{P_c}{J_2}}, \tag{16}$$

$$T_c = I_1 \zeta - I_2 \zeta^2, \tag{17}$$

where  $P_c = 2P / (\rho V^3 \pi R^2)$ .

Step 10: If the difference between new  $\zeta$  and old  $\zeta$  is not small enough, go to step 3.

Step 11: Calculate propeller efficiency ( $T_c/P_c$ ).

As described in Step 5, the performance of the propeller in the present method largely depends on the aerodynamic database of the adopted airfoil. Thus, it is important not only to use an airfoil with a good performance but also to construct an accurate aerodynamic database for the given airfoil. In

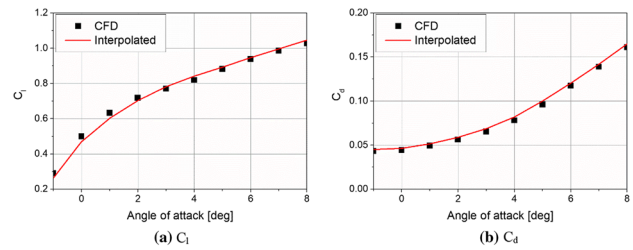


Fig. 6 Comparison of interpolated data with CFD result at  $M = 0.7$  and  $Re = 12,000$  where the calculated data does not exist in database

Table 2 Power consumption for various propeller designs

	Power (W)	Efficiency (%)
Propeller Designer	387.6	77.4
Present (XFOIL)	393.6	76.2
Present (TAS-PUG)	410.9	73.0

this study, TAS-PUG was used to construct the aerodynamic database of the airfoil used for the propeller design. The aerodynamic data used were acquired at uniform intervals over a specific range of Mach numbers, Reynolds numbers, and angles of attack. The data at flow conditions that were unavailable in the database were interpolated using the cubic spline method. Figure 6 shows the interpolated data at Mach and Reynolds numbers of 0.7 and 12,000, where the data do not exist in the database, with the data at Reynolds numbers of 10,000 and 14,000 and Mach numbers of 0.55 and 0.75 in the aerodynamic database constructed using TAS-PUG. The interpolated data show reasonable accuracy when compared with the CFD results by TAS-PUG.

To verify the propeller design code used in this study, the results were compared with those obtained using Propeller Designer [35]. The 1 m diameter propeller using the DAE-51 airfoil was designed to generate a thrust of 30 N at a free-flow speed of 10 m/s with 1500 rpm. The airfoil aerodynamic database was constructed using both the XFOIL and TAS-PUG. Table 2 and Fig. 7 depict the results of the propeller designs. All three propellers had similar shapes in terms of their chord length and twisting angle. The power consumption and efficiency of the propellers designed with XFOIL and Propeller Designer are predicted to be very similar. However, the propeller designed with the airfoil database constructed by TAS-PUG with the  $\gamma$ - $Re_\theta$  transition model consumes approximately 6% more power than the aforementioned two propellers because the drag coefficient estimated by TAS-PUG using the  $\gamma$ - $Re_\theta$  transition model is larger than that for the propeller designed with XFOIL. Because accurate power prediction is essential for the propeller design of Mars exploration aircraft, the database is constructed with TAS-PUG using the  $\gamma$ - $Re_\theta$  transition model in this study.

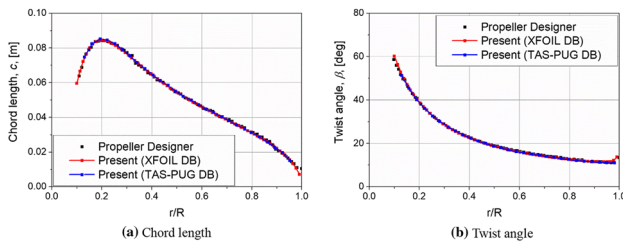


Fig. 7 Comparison of chord length and twist at each blade station of propellers

## 4 Multi-objective Optimization Airfoils for Propellers

### 4.1 Optimization Method

In this study, MOGA [36, 37] was used to determine the optimal airfoil shape accounting for multiple aerodynamic characteristics related to propeller performance of the Mars exploration aircraft. The genetic algorithm requires a large number of function calls as it involves population-based searches. In particular, the fitness evaluation method, in combination with the methods needing tremendous computational time, such as Navier–Stokes solver, leads to exorbitant computational costs. Therefore, in this study, RANS-based CFD simulation was used to evaluate the performance of only a specified number of sample points (airfoils), and the Kriging model that was constructed using this result was combined with MOGA to reduce the computational time.

Figure 8 shows a flowchart of the optimal airfoil design process used in this study. First, the 70 initial samples that were uniformly distributed in the design space were extracted using Latin hypercube sampling (LHS); these are depicted in Fig. 9.

### 4.2 Definition of the Airfoil Optimization Problem

In this study, the propeller specifications for the Mars exploration aircraft were determined based on a previous study on the conceptual design of the Mars exploration aircraft, as shown in Fig. 10 and Table 3. The rotation speed of the propeller was set to 1400 rpm considering the aircraft cruising speed and propeller tip speed, and its diameter of the propeller was set to 1.9 m under the assumption that the aircraft was mounted on a Viking shell [38] and transported to Mars. Since operational reliability is vital for Martian missions and the aerodynamic performance of such aircraft is apt to deteriorate in the Martian atmosphere, two fixed-pitch propellers with four blades were selected as the design targets. The total required thrust of the propeller was 18.208 N, which required a thrust of 9.104 N per propeller.

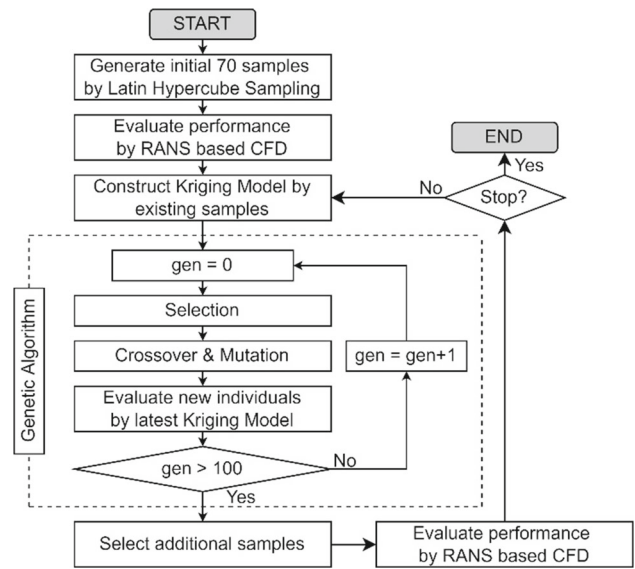
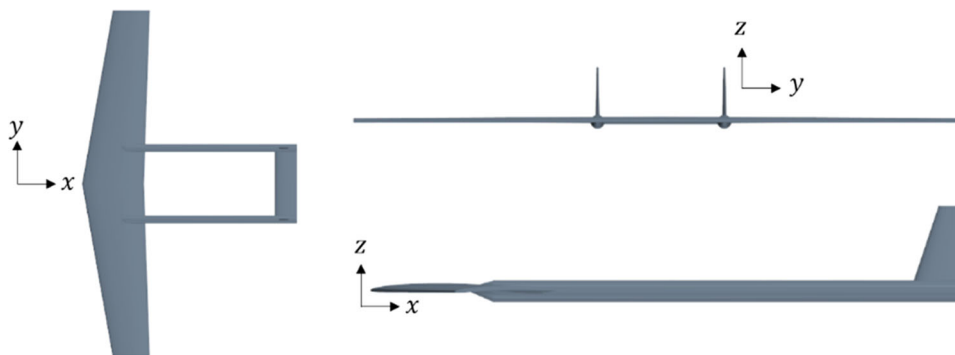


Fig. 8 Flowchart of the optimization process



Fig. 9 All 70 initial samples from the optimization process

**Fig. 10** Appearance of the Mars exploration aircraft



**Table 3** Specifications of Mars exploration aircraft and its propeller

Wing span of aircraft	7.75 m	Cruise AoA	3°
Weight of aircraft	75.2 kg	Cruise speed	111.1 m/s
Overall length of aircraft	4.582 m	Mach number	0.48
Reynolds number (Re)	141,100	Propeller type	Fixed pitch
Number of blades	4	Propeller rotational speed	1400 rpm
Propeller diameter	1.9 m	Required thrust (T)	18.208 N

Since the propeller was designed with the same airfoil across all blade stations, the flow conditions at the blade station where the maximum thrust and power is obtained was set as the conditions for airfoil optimization design. Turbulence intensity was determined using the flow velocity in Valles Marineris [32] predicted by the Mars Regional Atmospheric Modeling System (MRAMS), which predicts the atmospheric conditions on Mars. Therefore, the flow condition for airfoil design was characterized by a Mach number of 0.7, Reynolds number of 12,000, and turbulence intensity of 0.5%.

The airfoil shape was defined using a non-uniform rational basis spline (NURBS) curve, as shown in Fig. 11, to allow for a high degree of freedom. A total of 17 NURBS control points were used, which were expressed using a total of 28 variables. The ranges of the  $x$ -coordinate of control points (i.e.,  $dv_2$ ,  $dv_4$ ,  $dv_6$ , and so on) were set to not overlap with that of the neighbor control point to prevent unrealistic airfoil shapes, and the ranges of the  $y$ -coordinate were set by referring to the NURBS control points that represent ARA-D 6% airfoil. The lower and upper bounds of design variables are described in Table 4. Considering the structural strength of the propeller, the maximum thickness of the airfoil is constrained to be greater than 4% of the chord length.

Finally, the following three aerodynamic performances are selected as objective functions:

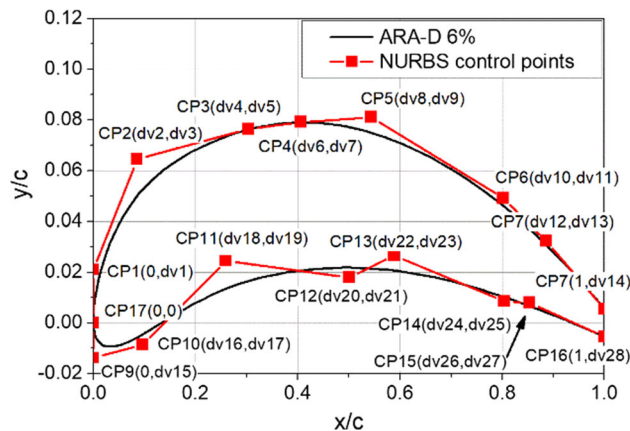


**Fig. 11** NURBS control points of an airfoil at the optimization

1. Maximization of the lift-to-drag ratio
2. Minimization of the drag coefficient at the angle of attack where the maximum lift-to-drag ratio is obtained
3. Minimization of the standard deviation of  $(dC_l)/d\alpha$  between 1° and 6° angle of attack

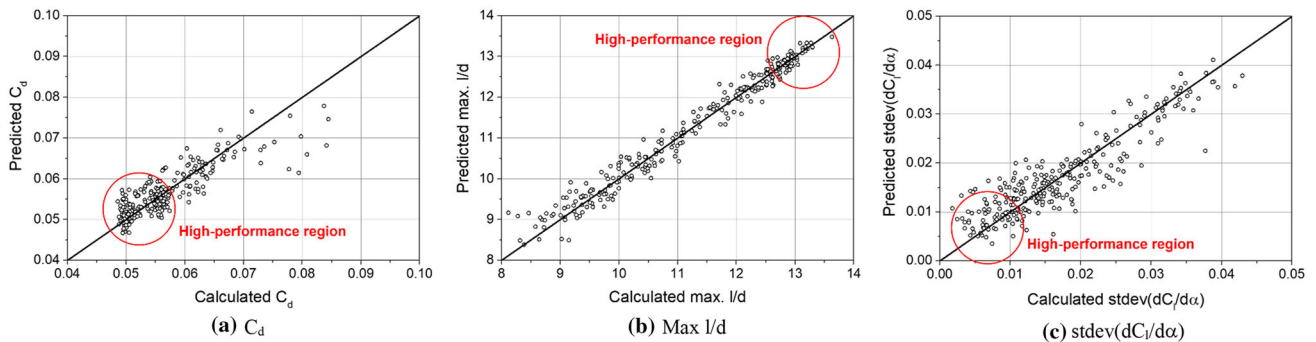
The first objective function is selected because the propeller design method used in this study finds the propeller shape which has the maximum lift-to-drag ratio at each blade station as described in Sect. 3. The second objective function is adopted to suppress the excessive increase of the drag at the condition where the maximum lift-to-drag ratio is obtained. The third objective function is selected to maintain stable aerodynamic performance under the environmental disturbances expected from the Martian atmosphere, which is characterized by frequent wind gusts.

### 4.3 Optimization Results

During the design process, the performances of a total of 288 airfoils, composed of 70 initial and 218 additional sample airfoils, were evaluated by TAS-PUG using the  $\gamma$ - $Re_\theta$  transition model. Total 27 kriging model update was conducted until the Pareto front of MOGA using Kriging model

**Table 4** The ranges of the design variables for airfoil optimization

	Upper surface		Lower surface		
	Lower bound	Upper bound	Lower bound	Upper bound	
dv1	0.02032	0.02897	dv15	− 0.01501	− 0.00117
dv2	0.00000	0.16000	dv16	0.00000	0.16000
dv3	0.04129	0.06888	dv17	− 0.00933	− 0.00150
dv4	0.16000	0.33000	dv18	0.16000	0.33000
dv5	0.06949	0.07729	dv19	0.00980	0.02584
dv6	0.33000	0.50000	dv20	0.33000	0.50000
dv7	0.05807	0.08143	dv21	0.00650	0.01894
dv8	0.50000	0.67000	dv22	0.50000	0.67000
dv9	0.07753	0.08159	dv23	0.02312	0.02688
dv10	0.67000	0.84000	dv24	0.67000	0.84000
dv11	0.03388	0.05032	dv25	0.00087	0.00936
dv12	0.84000	1.00000	dv26	0.84000	1.00000
dv13	0.01735	0.03359	dv27	0.00755	0.01182
dv14	0.00000	0.00550	dv28	− 0.00550	0.00000

**Fig. 12** Leave one cross-validation of the constructed Kriging model for each objective function

does not change anymore. With these results, the Kriging model is constructed for each objective function. Figure 12 shows the results of leave one out cross-validation results of the constructed Kriging models. In this figure, the horizontal axis is the calculated value by TAS–PUG using the  $\gamma$ - $Re_\theta$  transition model; the vertical axis is the predicted value by Kriging model. Even though there are some points at which its accuracy is not enough, the constructed Kriging model has a reliable accuracy as a whole. Especially, the Kriging model shows a relatively good accuracy near the high-performance region (high max.  $l/d$ , low  $C_d$ , and low  $dC_1/d\alpha$  region) because additional sample points were selected from the high-performance region in each iteration.

Figure 13 shows the results of plotting the objective function values of the 288 airfoils obtained through optimization. Compared to the 70 initial airfoils selected by LHS, the additional ones obtained through optimization were located in the areas of the improved objective functions. This indicates that the optimization algorithm works properly. The Pareto

front formed by airfoils obtained from optimization shows that there is a trade-off between each objective function. A compromised solution (OPT airfoil) for the three objective functions was selected among the Pareto solutions, and the performance of this airfoil was compared with that of the ARA-D 6% airfoil and the airfoil that was designed for the main wing of a Mars exploration aircraft [8]. Figure 14 shows the shape of each airfoil. OPT airfoil has a sharp leading edge with a thinner airfoil thickness, a flatter maximum camber shape which is located about mid-chord. These features correspond to the shape characteristic of airfoils with a good aerodynamic performance at low-Reynolds-flow conditions [39].

Table 5 shows the objective function values obtained under the design flow conditions. Figure 15 also compares the aerodynamic performance of each airfoil at angles of attack ranging from  $-3^\circ$  to  $20^\circ$ . When compared over a wide range of angles of attack as well as under the design flow conditions, these results demonstrate the superior performance of



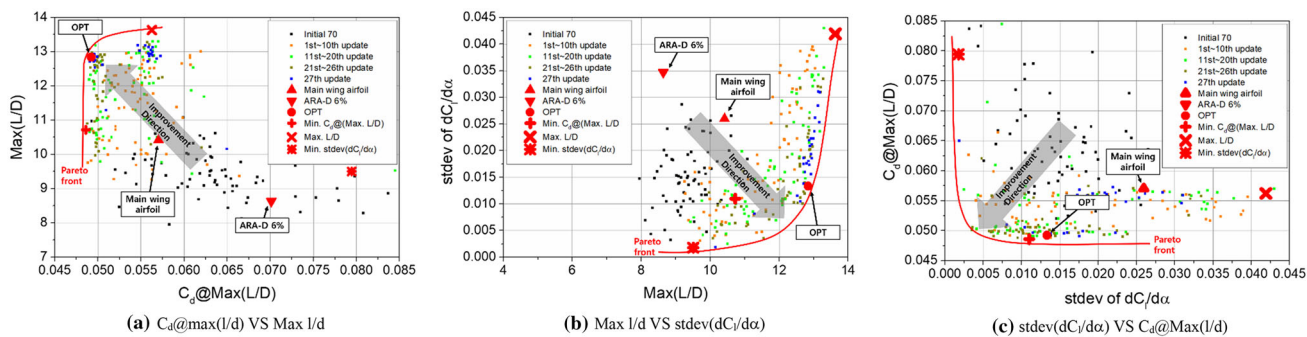


Fig. 13 Plots of objective functions of 288 airfoils obtained through the optimization process

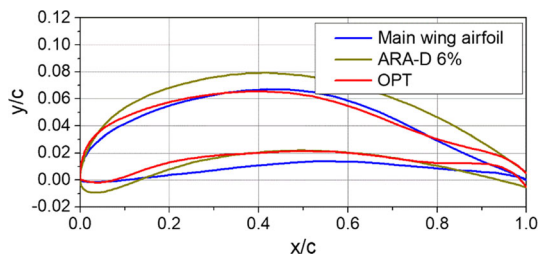


Fig. 14 Geometries of OPT and reference airfoils

Table 5 Objective functions of OPT and reference airfoils

	Max l/d	$C_d$ @ Max l/d	Stdev ( $dC_l/d\alpha$ )
Main-wing airfoil	10.41374	0.05704	0.02595
ARA-D 6%	8.63851	0.07011	0.03471
OPT	12.83759	0.04923	0.01332

the OPT airfoil obtained from optimization over the reference airfoils. Especially, it can be confirmed that OPT airfoil and Main-wing airfoil show a constant  $C_m$  at lower angle of attack.

It can be confirmed that the optimization process increases the maximum lift-to-drag ratio while decreasing the drag coefficient at the corresponding angle of attack. Rather than reducing the drag at a fixed angle of attack, the present optimization makes that the maximum lift-to-drag ratio occurs at

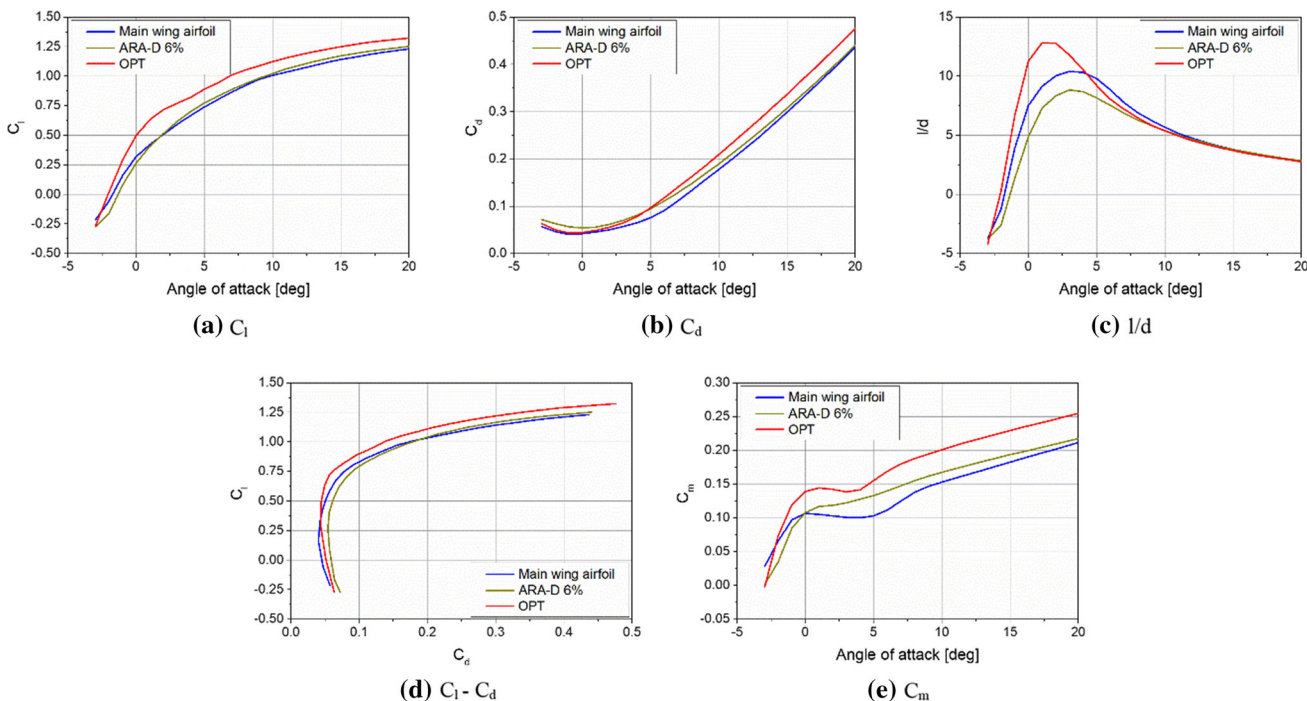
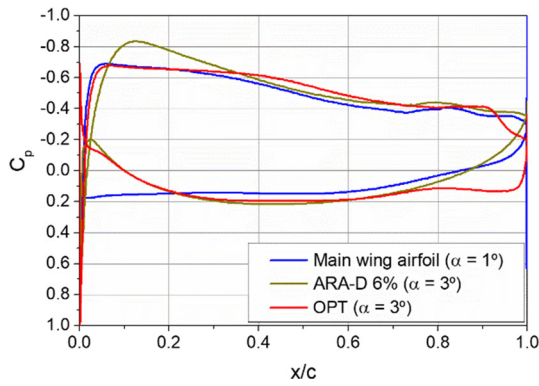


Fig. 15 Comparison of aerodynamic performances of the OPT and reference airfoils



**Fig. 16** Comparison of pressure coefficient of the OPT and reference airfoils at the angle of attack where maximum  $l/d$  occur for each airfoil

**Table 6** Separation and transition position of OPT and reference airfoils

	Separation	Transition
Main-wing airfoil	0.545	Full laminar
ARA-D 6%	0.492	Full laminar
OPT	0.595	Full laminar

a relatively small angle of attack region where the drag is not increased too much. Figure 16 compares the distribution of the pressure coefficient of the OPT and reference airfoils at the angle of attack where maximum lift-to-drag ratio occur for each airfoil. OPT airfoil show a flat upper surface pressure distribution which is the typical feature of laminar airfoil. This feature contributes to delay the separation at this angle of attack, as shown in Table 6. It is confirmed that the OPT airfoil generates more lift at trailing-edge region because of curved trailing-edge shape.

Next, propellers were designed with the ARA-D 6% airfoil, the main wing airfoil of the Mars exploration aircraft, and the OPT airfoil to investigate the performance of the propellers. The airfoil aerodynamic database used in the design of the propellers was constructed by TAS-PUG using the  $\gamma$ - $Re_\theta$  model. Figure 17 shows the planform geometry and twist angle distribution of the designed propellers.

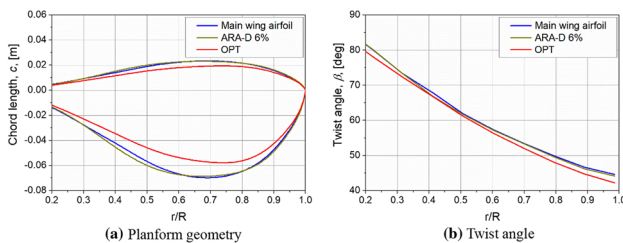


**Fig. 17** Planform geometry and twist angle distribution of the propellers

**Table 7** Power consumption and efficiency of the OPT and reference airfoil propellers

	Power (W)	Efficiency (%)
Main-wing airfoil	1313.841	76.985
ARA-D 6%	1349.971	74.924
OPT	1248.049	81.043

Table 7 shows the required power and efficiency of the propellers designed using the OPT and reference airfoils. The efficiency of the propeller with the OPT airfoil is improved by approximately 3–5% compared to the propeller designed using the two other reference airfoils. As shown in Fig. 17, the propeller designed using the OPT airfoil has a smaller chord length and twist angle compared to the propellers designed using the comparative reference airfoils. The propeller using the OPT airfoil produces the required thrust even with the small volume size. This fact may also be merit when mounting the Mars exploration airplane in the aero capsule.

#### 4.4 Data Mining Using the Optimization Results

To extract those characteristics of the designed airfoil that are related to its performance, such as its geometric features, the design results were analyzed using data-mining techniques, ANOVA and SOM.

##### 4.4.1 Analysis of Variance (ANOVA)

ANOVA is a commonly used statistical analysis method, which quantitatively identifies the degree of influence of an input variable on an output variable using the ratio of the variance due to each input variable to the total variance. The ANOVA employed in this study decomposes the total variance of the model into the variance due to the design variables on the Kriging model. Decomposition is performed by integrating output variables of model ( $\hat{y}$ ). The total mean ( $\hat{\mu}_{total}$ ) and the variance ( $\hat{\sigma}_{total}^2$ ) of the model are follows:

$$\hat{\mu}_{total} \equiv \int \cdots \int \hat{y}(x_1, \dots, x_m) dx_1 \cdots dx_m, \tag{18}$$

$$\hat{\sigma}_{total}^2 \equiv \int \cdots \int [\hat{y}(x_1, \dots, x_m) - \hat{\mu}_{total}]^2 dx_1 \cdots dx_m. \tag{19}$$

Herein,  $m$  is the number of design variables. The main effect of variable  $x_i$  is given as:

$$\hat{\mu}_i(x_i) \equiv \int \cdots \int \hat{y}(x_1, \dots, x_m) dx_1 \cdots dx_{i-1} dx_{i+1} \cdots dx_m - \hat{\mu}_{total}, \tag{20}$$

$\hat{\mu}_i(x_i)$  quantify the effect of variable  $x_i$  on the objective function.

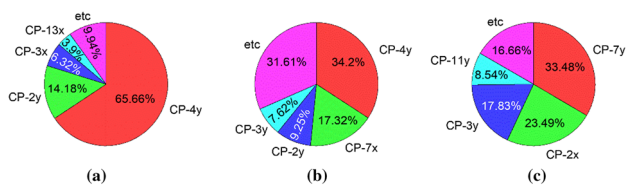


**Fig. 18** ANOVA results of the optimization process. **a** Max  $l/d$ ; **b**  $C_d@max\ l/d$ ; **c**  $cdev(dC_l/d\alpha)$

The variance due to the design variable  $x_i$  is given as:

$$\hat{\sigma}_i^2 \equiv \int [\hat{\mu}_i(x_i)]^2 dx_i. \tag{21}$$

The proportion of the variance due to design variable  $x_i$  to total variance of the model can be calculated by dividing Eq. (21) by Eq. (19):

$$\frac{\hat{\sigma}_i^2}{\hat{\sigma}_{total}^2} \equiv \frac{\int [\hat{\mu}_i(x_i)]^2 dx_i}{\int \dots \int [\hat{y}(x_1, \dots, x_m) - \hat{\mu}_{total}]^2 dx_1 \dots dx_m}. \tag{22}$$

This value indicates the effect of design variable  $x_i$  on the objective function.

Figure 18 shows the results obtained using ANOVA. The top four design variables with a high degree of influence on each objective function are shown. Each design variable is expressed in a form such as CP-5x, which indicates the  $x$ -coordinate of the NURBS control point No. 5. The four design variables with the most significant effect on the maximum lift-to-drag ratio are CP-4y (34.14%), CP-7x (17.29%), CP-2y (9.23%), and CP-3y (7.80%). The four design variables with the most significant effect on the drag coefficient at the maximum lift-to-drag ratio are CP-4y (65.66%), CP-2y (14.18%), CP-3x (6.32%), and CP-13x (3.90%). Finally, the four design variables with the most significant effect on the standard deviation of  $(dC_l)/(d\alpha)$  are CP-7y (33.48%), CP-2x (23.49%), and CP-3y (17.83%), and CP-11y (8.54%).

The arrows in Fig. 19 indicate the directions along which the objective function varies. Here, “A-direction” refers to the direction in which the objective function of the initial 70 airfoils improved to the objective function of the airfoils located at the center of the Pareto front. B- and C-directions are those in which the objective function of the airfoil located at the center of the Pareto front shifts to that of the airfoils located at both ends of the Pareto front (extreme solutions). Table 8 shows the increases and decreases (green: increase; orange: decrease) of the design variables that induce changes in each direction.

#### 4.4.2 Self-Organizing Map (SOM)

SOM is an unsupervised neural network technique that projects high-dimensional data into a low-dimensional space.

It qualitatively represents the relationship between the input and output variables or between the various input variables by classifying, organizing, and visualizing a large amount of data. The detailed learning algorithm of SOM can be referred to [18].

Figure 20 shows the SOM results with the 288 airfoils obtained during the optimization process. In this study, clustering is performed based on the objective function values of airfoils, and each map is colored by objective function value or design variable value. Thus, for example, it can be said that airfoils that have a small drag coefficient at the maximum lift-to-drag ratio and a large lift–drag ratio are located in the bottom-left corner of the map, while the airfoils that have a large drag coefficient at the maximum lift-to-drag ratio, a small lift-to-drag and a small  $(dC_l)/(d\alpha)$  are located in the upper-right corner of the map. The qualitative relationships between objective functions and design variables can be investigated by comparing the color arrangement between maps. For example, comparing the SOM of drag coefficients obtained at the maximum lift ratio with that of CP-4y, the color arrangement of these two maps is very similar. It means that the drag coefficient is small (blue) when the value of CP-4y is small (blue). The SOM of design variables that show a similar color arrangement with the SOM of the drag coefficient at the maximum lift-to-drag ratio were CP-4y, CP-5x, CP-5y, CP-6x, CP-6y, and CP-16y. The design variables that show a similar color arrangement with the SOM of the maximum lift-to-drag ratio itself were CP-1y, CP-4x, CP-8y, CP-9y, CP-14y, CP-15x, and CP-15y. Finally, the design variable that shows a similar color arrangement with the SOM of the standard deviation of the lift curve slope was CP-7y. In this manner, it is possible to extract relationships between objective functions and the design variables using SOM.

#### 4.4.3 Summary of Geometric Features Obtained by Data Mining

According to the ANOVA and SOM results, the key features of the airfoil shape required to improve each objective function can be summarized as follows:

1. The airfoils with a high lift-to-drag ratio performance have a sharp and large gradient leading edge, a thinner thickness, and a large camber. These are typical features of high-performance low-Reynolds-number airfoil. A sharp leading edge generates a high adverse pressure gradient at the leading edge, which results in flow separation and vortex shedding.
2. The airfoil with a low drag coefficient at the maximum lift-to-drag ratio have an increased gradient on the suction surface, which results in the sharply curved trailing-edge shape and reduction of thickness there. This feature increases the adverse pressure gradient at the trailing

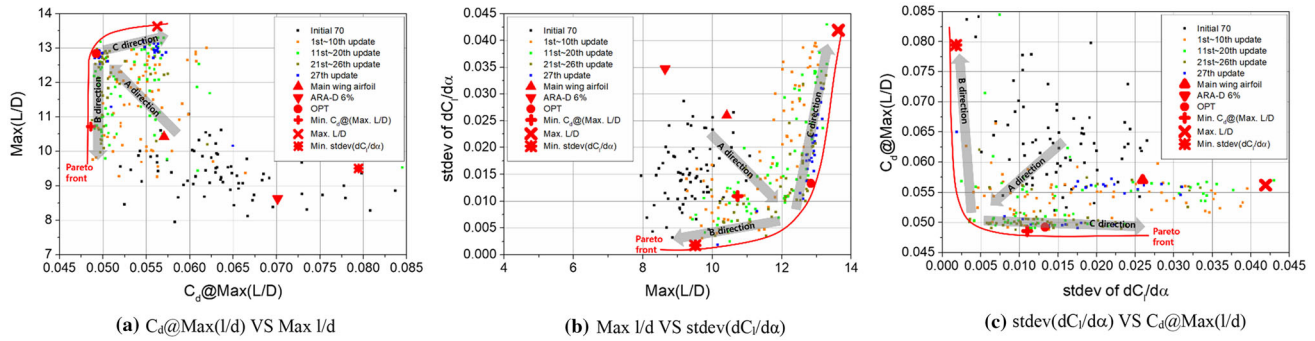


Fig. 19 Direction of the change of objectives near the Pareto front

**Table 8** Variation of design variables along the direction of change of objectives; increase (green color), decrease (orange color)

	A-direction		B-direction		C-direction	
Max l/d	CP-4y	CP-4y	CP-4y	CP-4y	CP-4y	CP-4y
	CP-7x	CP-2y	CP-7x	CP-2y	CP-7x	CP-2y
vs C <sub>d</sub> @Max l/d	CP-2y	CP-3x	CP-2y	CP-3x	CP-2y	CP-3x
	CP-3y	CP-13x	CP-3y	CP-13x	CP-3y	CP-13x
stdev(dC <sub>l</sub> /dα)	CP-7y	CP-4y	CP-7y	CP-4y	CP-7y	CP-4y
	CP-2x	CP-2y	CP-2x	CP-2y	CP-2x	CP-2y
vs Max l/d	CP-3y	CP-3x	CP-3y	CP-3x	CP-3y	CP-3x
	CP-11y	CP-13x	CP-11y	CP-13x	CP-11y	CP-13x
C <sub>d</sub> @Max l/d	CP-7y	CP-4y	CP-7y	CP-4y	CP-7y	CP-4y
	CP-2x	CP-7x	CP-2x	CP-7x	CP-2x	CP-7x
vs stdev(dC <sub>l</sub> /dα)	CP-3y	CP-2y	CP-3y	CP-2y	CP-3y	CP-2y
	CP-11y	CP-3y	CP-11y	CP-3y	CP-11y	CP-3y

edge and induces reattachment while reducing the pressure drag.

- The airfoil with a small standard deviation of  $(dC_l)/(\alpha)$  has a smooth curvature on the suction surface near the trailing edge. This feature delays the nonlinearity of  $C_l$  as long as possible.

### 5 Conclusion

This study aims to improve the aerodynamic performance of propellers for Mars exploration aircraft using multi-objective shape optimization to design propeller airfoils. To evaluate the performance of the airfoil operated in low-Reynolds-number and high-subsonic flows condition on Mars accurately, a Reynolds-averaged Navier–Stokes (RANS) simulation using the  $\gamma$ - $Re_\theta$  transition model were utilized to evaluate airfoil performance and construct a corresponding aerodynamic database for propeller design. To increase the degrees of freedom for the airfoil shape, the NURBS method was used to define the airfoil shape. MOGA was used to find the optimal solution (airfoil), and a Kriging model was used to reduce the computational

time. The propeller with the designed airfoil was determined using the Adkins method. Compared to propellers constructed using reference airfoils, the power consumption and efficiency of propellers with the designed airfoil were significantly improved. In addition, quantitative and qualitative correlations between various design variables and airfoil performance were analyzed using ANOVA and SOM to extract the geometric features that affect airfoil performance in the low Reynolds number flow condition on Mars. The airfoils with a high lift-to-drag ratio performance have a sharp and large gradient leading edge, a thinner thickness, and a large camber. The airfoils with a low drag coefficient at the maximum lift-to-drag ratio have an increased gradient of the suction surface, which results in the sharply curved trailing-edge shape and reduction of thickness there. The airfoil with a small standard deviation of  $dC_l/\alpha$  has a smooth curvature at the suction surface near the trailing edge. These shape features about the low-Reynolds-number airfoil will be helpful to understand the physics around the airfoil.

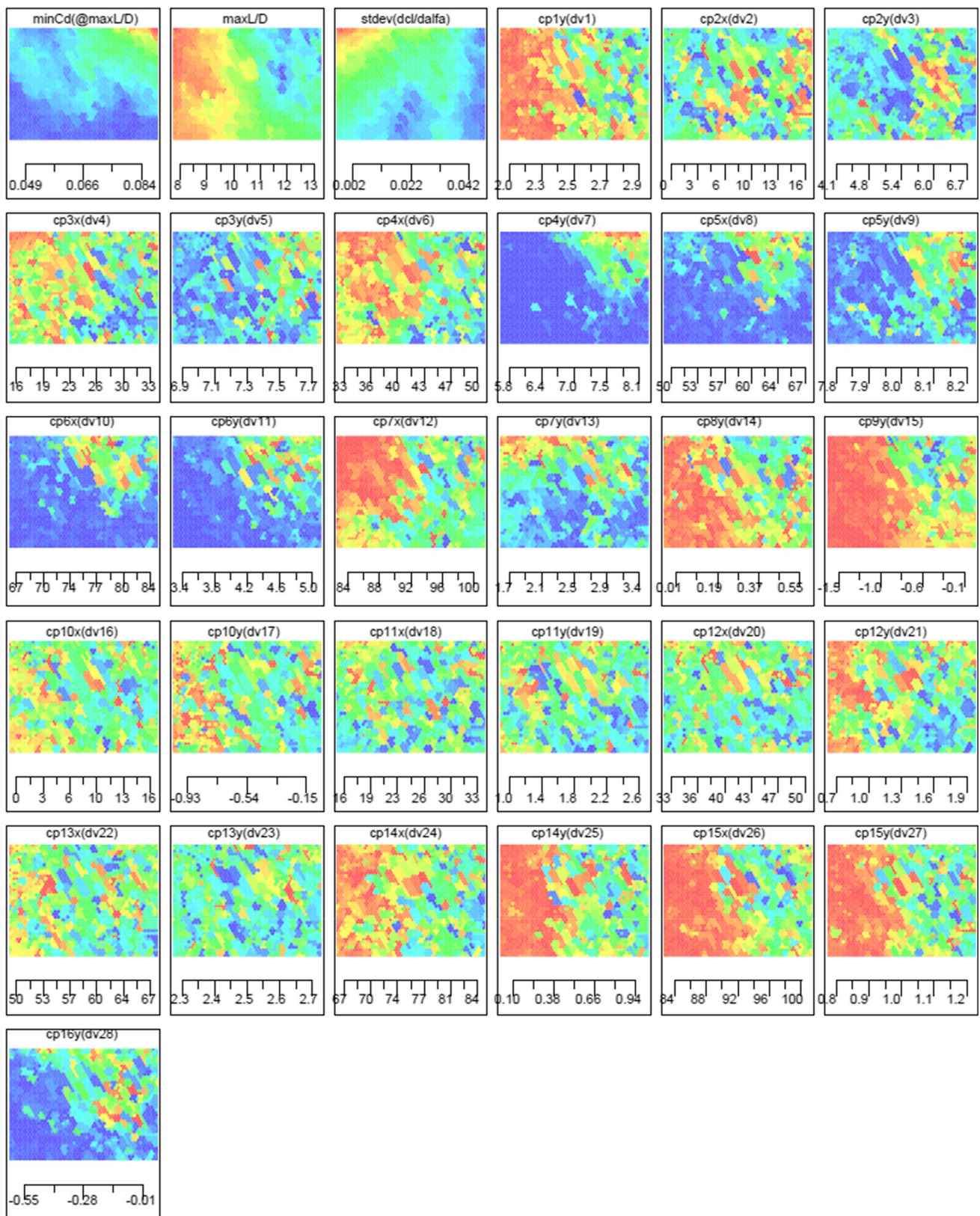


Fig. 20 SOM maps of the optimization variables

**Acknowledgements** The development of the optimization method was supported by a Grant (UE191109CD) from the Agency for Defense Development (ADD) and the Defense Acquisition Program Administration (DAPA) and the National Research Foundation of Korea (NRF) grant funded by the Korea government (MSIT) (no. NRF-2017M1A3A3A02016269).

## References

- Withrow-Maser S, Johnson W, Young L, Koning W, Kuang W, Malpica C, Balaram J, Tzanetos T (2020) Mars science helicopter: conceptual design of the next generation of mars rotorcraft. Accelerator space commercial exploration new discovery conference ASCEND 2020, pp 1–19
- Datta A, Roget B, Griffiths D, Pugliese G, Sitaraman J, Bao J, Liu L, Gamard O (2003) Design of a martian autonomous rotary-wing vehicle. *J Aircr* 40:461–472
- O'Brien P (2003) Using a robotic helicopter to fuel interest in and augment the human exploration of the planet Mars. In: AIAA space 2003 conference expo. <https://doi.org/10.2514/6.2003-6275>
- Fujita K, Karaca H, Nagai H (2020) Parametric study of Mars helicopter for pit crater exploration. AIAA Scitech 2020 Forum. <https://doi.org/10.2514/6.2020-1734>
- AME mission
- Braun RD, Wright HS, Croom MA, Levine JS, Spencer DA (2006) Design of the ARES mars airplane and mission architecture. *J Spacecr Rockets* 43:1026–1034
- Fujita K, Luong R, Nagai H, Asai K (2012) Conceptual design of mars airplane. *Trans Jpn Soc Aeron Space Sci Aerosp Technol Jpn* 10:Te\_5–Te\_10
- Jung J, Yee K, Misaka T, Jeong S (2017) Low Reynolds number airfoil design for a Mars exploration airplane using a transition model. *Trans Jpn Soc Aeron Space Sci* 60:333–340
- Ladson CL (1988) Effects of independent variation of Mach and Reynolds numbers on the low-speed aerodynamic characteristics of the NACA0012 airfoil section. NASA Tech Memo 4074, vol 14
- Laitone EV (1997) Wind tunnel tests of wings at Reynolds numbers below 70 000. *Exp Fluids* 23:405–409
- Smith S, Gynn M, Streett C, Beeler G (2003) Mars airplane airfoil design with application to ARES. In: 2nd AIAA 'Unmanned Unlimited' conference work exhibitions. <https://doi.org/10.2514/6.2003-6607>
- Oyama A, Fujii K (2006) A study on airfoil design for future mars airplane. In: 44th AIAA aerospace science meet exhibition, vol 23, pp 17793–17800
- Anyoji M, Nonomura T, Aono H, Oyama A, Fujii K, Nagai H, Asai K (2014) Computational and experimental analysis of a high-performance airfoil under low-Reynolds-number flow condition. *J Aircr* 51:1864–1872
- Anyoji M, Nose K, Ida S, Numata D, Nagai H, Asai K (2010) Low Reynolds number airfoil testing in a Mars wind tunnel. In: 40th fluid dynamics conference exhibition. <https://doi.org/10.2514/6.2010-4627>
- Castelli MR, Garbo F, Benini E (2011) Numerical investigation of laminar to turbulent boundary layer transition on a Naca 0012 airfoil for vertical-axis wind turbine applications. *Wind Eng* 35:661–685
- Koning WJF, Romander EA, Johnson W (2020) Optimization of low Reynolds number airfoils for Martian rotor applications using an evolutionary algorithm. In: AIAA Scitech 2020 forum. <https://doi.org/10.2514/6.2020-0084>
- Jeong S, Shimoyama K (2011) Review of data mining for multidisciplinary design optimization. *Proc Inst Mech Eng Part G J Aerosp Eng* 225:469–479
- Jeong S, Chiba K, Obayashi S (2005) Data mining for aerodynamic design space. *J Aerosp Comput Inf Commun* 2:452–469
- Chiba K, Obayashi S (2007) Data mining for multidisciplinary design space of regional-jet wing. *J Aerosp Comput Inf Commun* 4:1019–1036
- Oyama A, Okabe Y, Shimoyama K, Fujii K (2009) Aerodynamic multiobjective design exploration of a flapping airfoil using a Navier–Stokes solver. *J Aerosp Comput Inf Commun* 6:256–270
- Jones DR, Schonlau M, Welch WJ (1998) Efficient global optimization of expensive black-box functions. *J Glob Optim* 13:455–492
- Kohonen T (1997) Self-organizing maps. Springer, Berlin
- Nakahashi K, Ito Y, Togashi F (2003) Some challenges of realistic flow simulations by unstructured grid CFD. *Int J Numer Methods Fluids* 43:769–783
- Venkatakrishnan V (1993) On the accuracy of limiters and convergence to steady state solutions. In: 31st aerospace science meeting and exhibition. <https://doi.org/10.2514/6.1993-880>
- Sharov D, Nakahashi K (1998) Reordering of hybrid unstructured grids for lower-upper symmetric gauss-seidel computations. *AIAA J* 36:484–486
- Menter FR, Langtry RB, Likki SR, Suzen YB, Huang PG, Völker S (2006) A correlation-based transition model using local variables—part I: model formulation. *J Turbomach* 128:413
- Langtry RB, Menter FR, Likki SR, Suzen YB, Huang PG, Völker S (2006) A correlation-based transition model using local variables—part II: test cases and industrial applications. *J Turbomach* 128:423–434
- Misaka T, Obayashi S (2006) Application of local correlation-based transition model to flows around wings. In: Collect technical paper—44th AIAA aerospace science meeting, vol 15, pp 10973–10983
- Counsil JNN, Boulama KG (2011) Validation of a low-cost transitional turbulence model for low-reynolds-number external aerodynamics. In: 20th AIAA computing fluid dynamics conference 2011, pp 1–25. <https://doi.org/10.2514/6.2011-3698>
- Shan H, Jiang L, Liu C (2005) Direct numerical simulation of flow separation around a NACA 0012 airfoil. *Comput Fluids* 34:1096–1114
- Adkins CN, Liebeck RH (1994) Design of optimum propellers. *J Propuls Power* 10:676–682
- Glauert H (1935). Airplane propellers. In: Aerodynamics theory, pp 169–360. [https://doi.org/10.1007/978-3-642-91487-4\\_3](https://doi.org/10.1007/978-3-642-91487-4_3)
- Theodorsen T (1948) Theory of propellers. McGraw-Hill, New York

34. Goldstein S (1929) On the vortex theory of screw propellers. *Proc R Soc Lond Ser A Contain Pap A Math Phys Character* 123:440–465
35. Park D, Lee Y, Cho T, Kim C (2018) Design and performance evaluation of propeller for solar-powered high-altitude long-endurance unmanned aerial vehicle. *Int J Aerosp Eng* 2018:1–23
36. Holland JH (1992) Genetic algorithms. *Sci Am* 267:66–73
37. Jeong S, Minemura Y, Obayashi S (2006) Optimization of combustion chamber for diesel engine using Kriging model. *J Fluid Sci Technol* 1:138–146
38. Potter DF, Karl S, Lambert M, Hannemann K (2013) Computation of radiative and convective contributions to Viking afterbody heating. In: 44th AIAA thermophysics conference. <https://doi.org/10.2514/6.2013-2895>
39. Sunada S, Sakaguchi A, Kawachi K (1997) Airfoil section characteristics at a low Reynolds number. *J Fluids Eng* 119:129–135

**Publisher's Note** Springer Nature remains neutral with regard to jurisdictional claims in published maps and institutional affiliations.

Springer Nature or its licensor holds exclusive rights to this article under a publishing agreement with the author(s) or other rightsholder(s); author self-archiving of the accepted manuscript version of this article is solely governed by the terms of such publishing agreement and applicable law.